What is a deep defect? Combining Shockley-Read-Hall statistics with multiphonon recombination theory

Basita Das,[1] Irene Aguilera,[1] Uwe Rau,[1] and Thomas Kirchartz[1,2]
[1]*IEK5-Photovoltaik, Forschungszentrum Jülich, 52425 Jülich, Germany*
[2]*Faculty of Engineering and CENIDE, University of Duisburg-Essen, Carl-Benz-Str. 199, 47057 Duisburg, Germany*

(Received 25 November 2019; revised manuscript received 15 January 2020; accepted 30 January 2020; published 26 February 2020)

Slow nonradiative recombination is a key factor in achieving high open-circuit voltages or high luminescence yields in any optoelectronic material. Whether a defect is contributing substantially to nonradiative recombination is often estimated by defect statistics based on the model by Shockley, Read, and Hall. However, defect statistics are agnostic to the origin of the capture coefficients and therefore conclude that essentially every defect between the two quasi-Fermi levels is equally likely to be a recombination-active defect. Here, we combine Shockley-Read-Hall statistics with microscopic models for defect-assisted recombination to study how the microscopic properties of a material affect how recombination active a defect is depending on its energy level. We then use material parameters representative of typical photovoltaic absorber materials ($CH_3NH_3PbI_3$, Si, and GaAs) to illustrate the relevance, but also the limitations of our model.

DOI: 10.1103/PhysRevMaterials.4.024602

I. INTRODUCTION

One of the key requirements for all optoelectronic devices is that conversion of energy between photons and excited electronic states is efficient while conversion of energy into heat must be minimized. In many cases, this statement has essentially boiled down to the requirement that nonradiative recombination in the bulk and at surfaces and interfaces of the semiconductors used for these devices must be minimized. Nonradiative recombination happens primarily via two different mechanisms, namely, Auger recombination and defect-assisted recombination [1–5] typically involving the emission of multiple phonons [6–12]. Auger recombination is of particular importance for high charge-carrier densities, achieved, for instance, by high doping concentrations or under high optical excitation as found, e.g., in concentrator solar cells. In many situations, where novel semiconductors are developed for applications in optoelectronics, recombination via defects is more important. Defects have been important, e.g., in the development of blue lasers based on GaN and InGaN [13], but they may also limit the performance of crystalline Si solar cells by their presence at the interface between the Si wafer and the contact layers [14–16]. Thus, the study of defects has in the past been an important aspect of semiconductor physics, and passivation of defects in different technologies had a crucial impact on their use for various applications in optoelectronics.

Defects are often categorized into deep and shallow defects. Shallow defects may slow down transport by trapping and releasing charge carriers and shallow defects with the right charge states (acceptorlike defects close to the valence band and donorlike defects close to the conduction band) may dope the semiconductor and thereby allow the formation of junctions that are crucial for the electronic and optoelectronic functionality of many devices. Deep defects, however, capture carriers from the bands and these captured carriers have (at room temperature or below) a fairly low likelihood of being excited to the conduction band (electrons) or valence band (holes), because the trap depth is much larger than the thermal energy k_BT. These defects may be recombination active [17–20], but it is not clear *a priori* whether we may expect all defects more than a few k_BT away from the nearest band edge to be highly recombination active.

The definition of what a deep trap really is may vary depending on the criterion used. For instance, Ref. [21] uses the extent of the defect wave function relative to the length scale of atomic bonds as a means of defining "deep." Here, the more localized the defect wave function, the more the adjective "deep" is appropriate. These rather loose definitions may, however, not necessarily serve the purpose of allowing us to quantify their expected impact on recombination. Thus, the purpose of the present paper is to answer the question of what a deep defect is by discussing under which circumstances a defect is likely to substantially affect the recombination. Theories for recombination via defects have been developed over the years [6–12,22–24] and we use them to study the defect-mediated recombination process in methylammonium lead triiodide (MAPI) [25–27]. We discuss the trap energy dependence of defect localization and its effect on the recombination activity of trap levels. We used trap energy dependence of recombination efficiency η_R to quantify the recombination activity of the defects. The defect levels with relatively high recombination activity are classified as deep defects since these are most detrimental to device performance. We also compare the recombination efficiency of MAPI to that of GaAs and Si to study the effect of different electron-phonon coupling mechanisms on defect-mediated recombination. In

addition, we compare recombination lifetimes of MAPI and GaAs to explain the long nonradiative lifetimes in MAPI [28].

The current study is useful for understanding the origin and energy level dependence of recombination coefficients or capture cross sections and the implications of these dependences on trap occupation and recombination rates. This is of particular importance, because recombination coefficients are typically used as fitting parameters for the analysis of experimental data originating from, e.g., transient spectroscopy [29,30], defect spectroscopy using capacitance-based methods [31], or drift-diffusion simulations applied to solar cells or other optoelectronic devices [32,33]. *Ab initio* calculations of recombination coefficients do exist but typically only for specific defects [34–39] in certain relevant materials. In addition, the current work will be helpful for the purposes of computational material screening [40–42], where previous work established [43] the role of nonradiative recombination as the key aspect for which to screen well-absorbing semiconductors.

The work is organized in the following order. Section II explains the theory of defect-assisted recombination and is divided into the following subsections. Section II A makes an introduction to the state-of-art statistical model of the defect-mediated recombination. Section II B then presents a concise microscopic theory for capture of carriers by defects more than a few k_BT away from either of the bands. Section II B 1 introduces the readers to the underlying physics of capture with the help of a configuration coordinate diagram presented in Fig. 3. Section II B 2 presents the analytical model of the microscopic theory of capture and lists all the expressions necessary to obtain the trap energy dependent capture coefficients in Table II. Section III illustrates the results highlighting the idea that not all defects are equally recombination active. The trap energy dependent capture coefficients are the fundamental parameters calculated in the current work and readily improves our understanding of what really is a deep defect. Section IV concludes the work by discussing the new insights it adds to the community and the limitations of the model presented.

II. THEORY OF DEFECT-ASSISTED RECOMBINATION

The rate of recombination via a defect depends on a range of properties: (i) capture coefficients $k_{n/p}$, in units of cm^3/s, describe how quickly the capture of electrons or holes in this defect takes place; (ii) the defect density N_T, in cm^{-3}, translates the capture coefficients $k_{n/p}$ into a lifetime $\tau_{n/p}$ such that $\tau_{n/p} = (k_{n/p}N_T)^{-1}$; and (iii) a recombination statistic translates all capture and emission processes into an occupation probability f_T for the defect and finally a total recombination rate. Depending on the possible charge states of the defect, there are different recombination statistics in use. For a singly charged defect that is either positive or neutral (donorlike) or negative or neutral (acceptorlike), Shockley-Read-Hall (SRH) statistics [3,4] is used, while for amphoteric defects that can be positive, neutral or negative Sah-Shockley [1] statistics is used.

The recombination statistics determines the occupation probability of the defect by considering the electron and hole concentrations and the values of the capture coefficients $k_{n/p}$. However, the recombination statistics makes no theoretical prediction of the expected magnitude of $k_{n/p}$. Therefore, to obtain an estimate of how defects will affect recombination, we need to understand both the recombination statistics and the microscopic origin of the capture coefficients. Thus, in the next two sections we will briefly review the basic idea of SRH statistics and the theory of electronic transitions between a band state and a defect state. By combining both, we obtain recombination efficiency as a function of the energetic position of a trap in a device.

A. Shockley-Read-Hall statistics and the Simmons and Taylor approximation

Shockley, Read [3], and Hall [4] described the recombination process via a singly charged defect as a combination of four separate processes: (1) electron capture, (2) electron emission, (3) hole capture, and (4) hole emission, as illustrated in Fig. 1(a). The rates and coefficients of the individual processes are schematically represented in Fig. 1(b). The mathematical forms of the rates and coefficients are given in Table I, where n/p are the electron/hole concentration, $\sigma_{n/p}$ are electron/hole capture cross section, v_{th} is the thermal velocity of carriers, and f_T is trap occupation probability by an electron, the hole counterpart of which is $(1 - f_T)$. At thermal equilibrium, the rate of capture equals the rate of emission for both carriers, and thus by principle of detailed balance [44] we obtain the emission coefficients for electrons e_n and holes e_p from k_n and k_p, respectively. At thermal equilibrium, f_T of a trap state at energy E_T is given by the Fermi-Dirac distribution $f_T = 1/\{1 + \exp[(E_T - E_F)/k_BT]\}$ and the effective density of states for electrons N_C and for holes N_V are taken equal to $2[(2\pi m^* k_B T)/h^2]^{3/2}$ by assuming equal effective mass m^* for electrons in the conduction band and holes in the valence band. The processes of capture and emission for electrons and holes have opposite effects on the state of occupation of the defect state, and f_T can also be expressed as the ratio of coefficients of the favorable processes to all possible processes [45] via

$$f_T = \frac{nk_n + e_p}{nk_n + pk_p + e_n + e_p}. \tag{1}$$

At steady state, the net rate of capture of electrons and holes are equal, $r_1 - r_2 = r_3 - r_4$, and f_T of the trap remains unchanged. Therefore, substituting f_T from Eq. (1) to the rates given in Table I, the rate of recombination $R_{SRH} = r_1 - r_2 = r_3 - r_4$ for a trap density N_T at a trap energy E_T is

$$R_{SRH} = N_T \eta_R, \tag{2}$$

where the net recombination efficiency η_R for a single trap at E_T is

$$\eta_R = \left[\frac{k_n k_p (np - n_0 p_0)}{nk_n + pk_p + e_n + e_p}\right], \tag{3}$$

and n_0/p_0 are the electron/hole equilibrium concentration.

Even though $k_{n/p}$ should depend on the position and charge state of the defect as we will see in the next section, for now, to illuminate upon the idea of whether a defect at energy E_T will act as a recombination center or not, we consider constant $k_{n/p}$

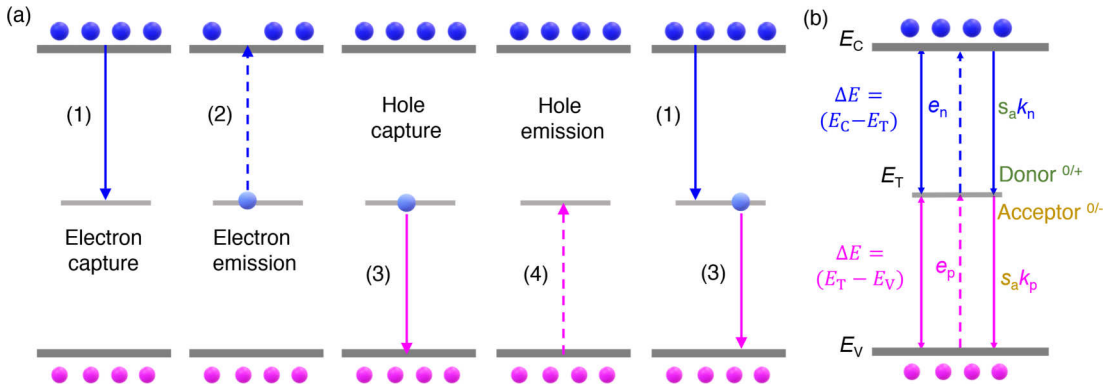

FIG. 1. SRH statistics is the carrier statistics for a defect state determined from considering four different processes. The arrows always point in the direction of electron transition. (a) The four different processes are shown. Process (1) is electron capture by a defect state, process (2) is electron emission from a defect state, process (3) is hole capture, and process (4) is hole emission. Two subsequent capture processes result in recombination of an electron and hole. (b) Shows the electron capture coefficient k_n, hole capture coefficient k_p, electron emission coefficient e_n, and hole emission coefficient e_p. To include the effects of Coulomb interaction, Sommerfeld factor s_a is multiplied to the capture coefficient when the charge of the defect and the carrier it captures is opposite in nature. E_T is the trap energy and ΔE measures the energy difference between the defect level and the band state associated with the particular transition.

and a high injection of carriers such that $n = p$. In Fig. 2(a), we plot f_T as a function of trap position $E_T - E_V$ for constant $k_n = k_p = 10^{-9}\,\mathrm{cm}^3/\mathrm{s}$ and vary the applied voltage V_A from 0.1 to 1 V. For such an applied voltage V_A, the electron and hole concentrations are assumed to be given by

$$n = p = n_i^2 \exp\left[\frac{qV_A}{2k_B T}\right], \tag{4}$$

where

$$n_i = \sqrt{N_C N_V} \exp\left[\frac{-E_g}{2k_B T}\right]. \tag{5}$$

The trap occupation probability f_T so obtained is similar to the Fermi-Dirac distribution but features a plateau at $f_T \approx nk_n/(nk_n + pk_p) = 0.5$, approximately between the electron quasi-Fermi level E_{fn} and hole quasi-Fermi level E_{fp}. The behavior of f_T follows intuitively from Fig. 2(b) which represents k_n, k_p, e_n, e_p, and the normalized recombination efficiency η_R as a function of trap position $E_T - E_V$ for $V_A = 1.0$ V. It shows that when $E_V < E_T - E_V < E_{fp}$, e_p dominates over all the other coefficients, whereas the same is true for e_n when $E_{fn} < E_T - E_V < E_C$. When $E_{fp} < E_T - E_V < E_{fn}$, $k_{n/p} \gg e_{n/p}$ and since $k_n = k_p$, $f_T \sim 0.5$. This implies that when the defect is close to either of the bands, the trapped charges easily escape to their respective bands by thermal excitation but as the distance from either band edge increases, the rate of thermal emission $e_{n/p}$ decreases and the defect interacts with both bands only through carrier capture, thus behaving as a recombination center. This idea is further reinforced by the plot of normalized η_R in Fig. 2(c), which reaches a maximum for $E_{fp} < E_T - E_V < E_{fn}$ and decreases rapidly beyond that. This is the essential idea of the Simmons and Taylor (ST) approximation [5], which identifies the traps between the two quasi-Fermi levels as the most important recombination centers because the majority of the recombination happens via defects in this energy range. The ST approximation finds extensive usage in solar-cell device simulation thanks to the simplifications it allows in the trap energy dependence of trap occupation probability and recombination efficiency [46–48]. In Figs. 2(d), 2(e), and 2(f), we illustrate the effect of the capture kinetics on f_T, normalized η_R (normalized by the highest value of η_R when $k_n = k_p = 10^{-9}\,\mathrm{cm}^3/\mathrm{s}$), and the SRH lifetime τ_{eff}, respectively, by varying k_n and k_p. In Fig. 2(d), between E_{fp} and E_{fn}, when $k_p > k_n$ ($k_n/k_p = 0.25$ and 0.50), the trap is more likely to be empty, i.e., $(1 - f_T > f_T)$ with $(f_T < 0.5)$, whereas the trap is more likely to be occupied by an electron, i.e., $(1 - f_T < f_T)$ with $(f_T > 0.5)$, when $k_p < k_n$ ($k_n/k_p = 2$ and 4). Also, in Figs. 2(e) and 2(f), we see that if we reduce either k_n or k_p by the same factor we obtain the same normalized recombination efficiency η_R and SRH lifetime τ_{eff}. This is because the slower of the two capture rates always limits the recombination efficiency and improves either the electron or hole capture lifetimes defined as $\tau_{n/p} = (N_T k_{n/p})^{-1}$. The SRH recombination rate is directly affected by the recombination efficiency and the diminished R_{SRH} then improves the effective SRH lifetime given as $\tau_{eff} = n/R_{SRH}$. In a forward-bias and high-injection case, the SRH lifetime can be directly calculated as $\tau_{eff} = (\tau_n{}^{-1} + \tau_p{}^{-1})^{-1}$.

Now that we have established an idea of deep defects within the purview of SRH statistics, it is time to delve deeper into the microscopic picture of carrier capture to understand how the coefficients might vary with the energy of the defect.

TABLE I. Expression for capture rates, emission rates, and coefficients of a trap state.

Process	Rates	Coefficients
Electron capture	$r_1 = nk_n N_T(1 - f_T)$	$k_n = v_{th}\sigma_n$
Electron emission	$r_2 = e_n N_T f_T$	$e_n = k_n N_C \exp\left[\frac{E_T - E_C}{k_B T}\right]$
Hole capture	$r_3 = pk_p N_T f_T$	$k_p = v_{th}\sigma_p$
Hole emission	$r_4 = e_p N_T(1 - f_T)$	$e_p = k_p N_V \exp\left[\frac{E_V - E_T}{k_B T}\right]$

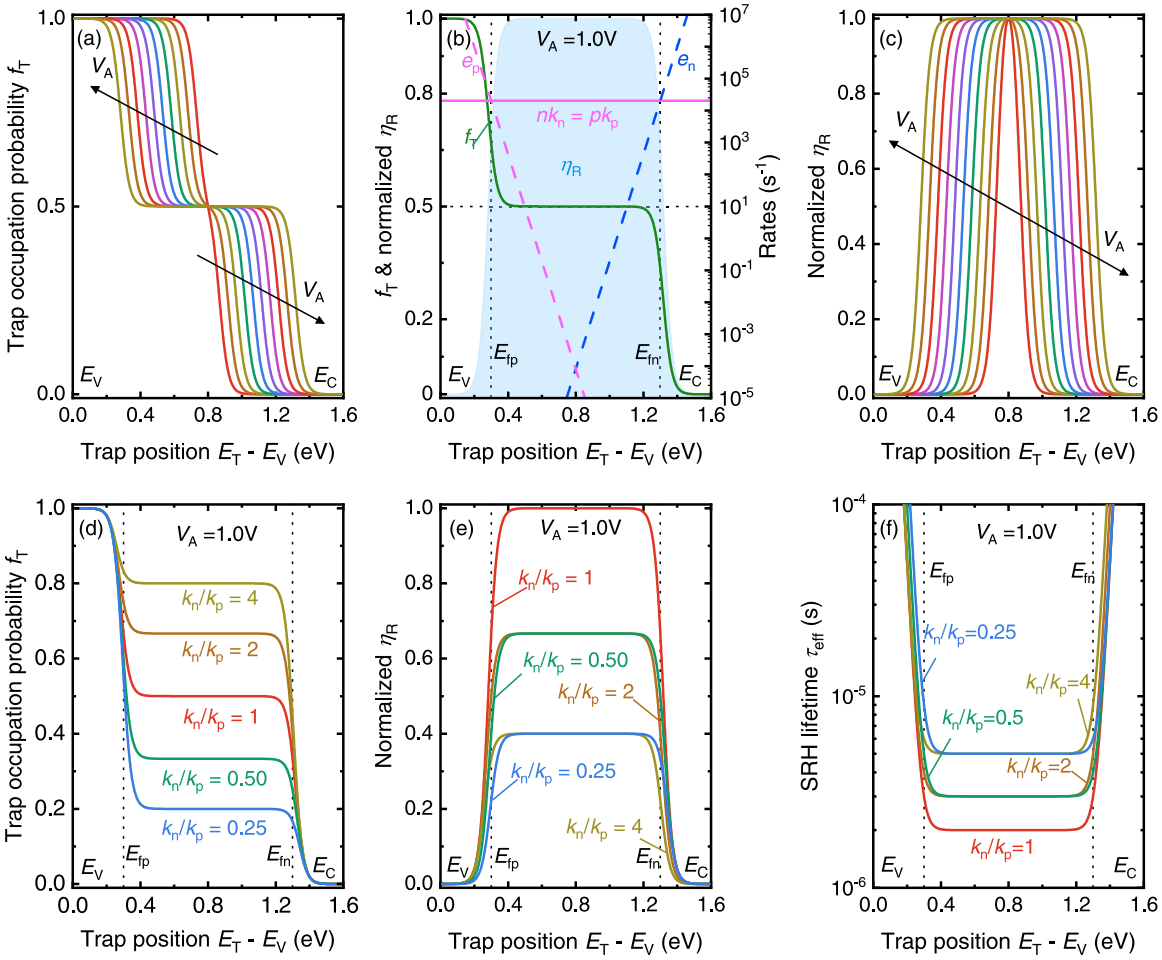

FIG. 2. Trap position dependence of trap occupation probability and recombination efficiency in MAPI is plotted for constant capture coefficients. (a) Trap occupation probability f_T plotted as a function of trap position for constant and equal capture coefficients $k_{n/p} = 10^{-9}\,\mathrm{cm}^3/\mathrm{s}$ at applied voltage V_A varied from 0.1 to 1.0 V in steps of 0.1 V. (b) The coefficients k_n, k_p, e_n, and e_p plotted for $V_A = 1.0\,\mathrm{V}$ along with f_T and the normalized recombination efficiency η_R. (c) Normalized η_R as a function of $E_T - E_V$ with varying V_A. (d) Occupation probability f_T for variable k_n and k_p (reduced from $k_{n/p} = 10^{-9}\,\mathrm{cm}^3/\mathrm{s}$) and $V_A = 1.0\,\mathrm{V}$. (e) Normalized η_R for varying k_n and k_p at $V_A = 1.0\,\mathrm{V}$. (f) SRH lifetime τ_{eff} in [s] for variable k_n and k_p at $V_A = 1.0\,\mathrm{V}$.

B. Microscopic understanding of carrier capture

The process of capture by a deep defect can happen either nonradiatively with the participation of multiple phonons (nonradiative multiphonon) [6–12] or radiatively by emission of a single photon and often accompanied by some phonons (radiative multiphonon) [22–24]. The probability of each such transition $W_{1,2}$ in s^{-1} from state $|1\rangle \rightarrow |2\rangle$ is calculated using Fermi's golden rule, via

$$W_{1,2} = \frac{2\pi}{\hbar}|M_{1,2}|^2 V N(E_2), \quad M_{1,2} = \langle \Psi_1 | \hat{H}_{\mathrm{int}} | \Psi_2 \rangle, \qquad (6)$$

where $M_{1,2}$ is the matrix element and gives the probability of the interaction between the initial state $|1\rangle$ and final state $|2\rangle$ due to the interaction Hamiltonian $\hat{H}_{\mathrm{int}}$, V is the volume of the system, and $N(E_2)$ is the final-state density of states. The instantaneous shape (position of the electrons and nuclei with respect to each other) of the initial state and final state are described by wave functions Ψ_1 and Ψ_2, respectively. The coefficients k_n or k_p of each such transition are related to the transition probability [49] by

$$k_{n/p} = W_{1,2}\, V. \qquad (7)$$

Thus, $k_{n/p}$ are not material constants but depend on the microscopic definition of the system given by the wave functions, the interaction Hamiltonian, and density of states. To understand the microscopic origin of $k_{n/p}$, a schematic representation of the individual processes is essential and the configuration coordinate (CC) diagram provides a good starting point to our discussion.

1. Configuration coordinate diagram

In a CC diagram [50], Fig. 3(a), we draw the total energy of an electron-lattice system as a function of dimensionless configurational coordinates Q normalized [49] as $Q = \sqrt{\frac{M\omega}{\hbar}}X$, where X represents the displacement of the lattice particles from their equilibrium position (the lowest energy point), M is mass of the unit cell, and ω is the angular frequency. In the dimensionless notation, Q replaces X and the equilibrium position of the lattice in the ith state is identified by Q_i. The

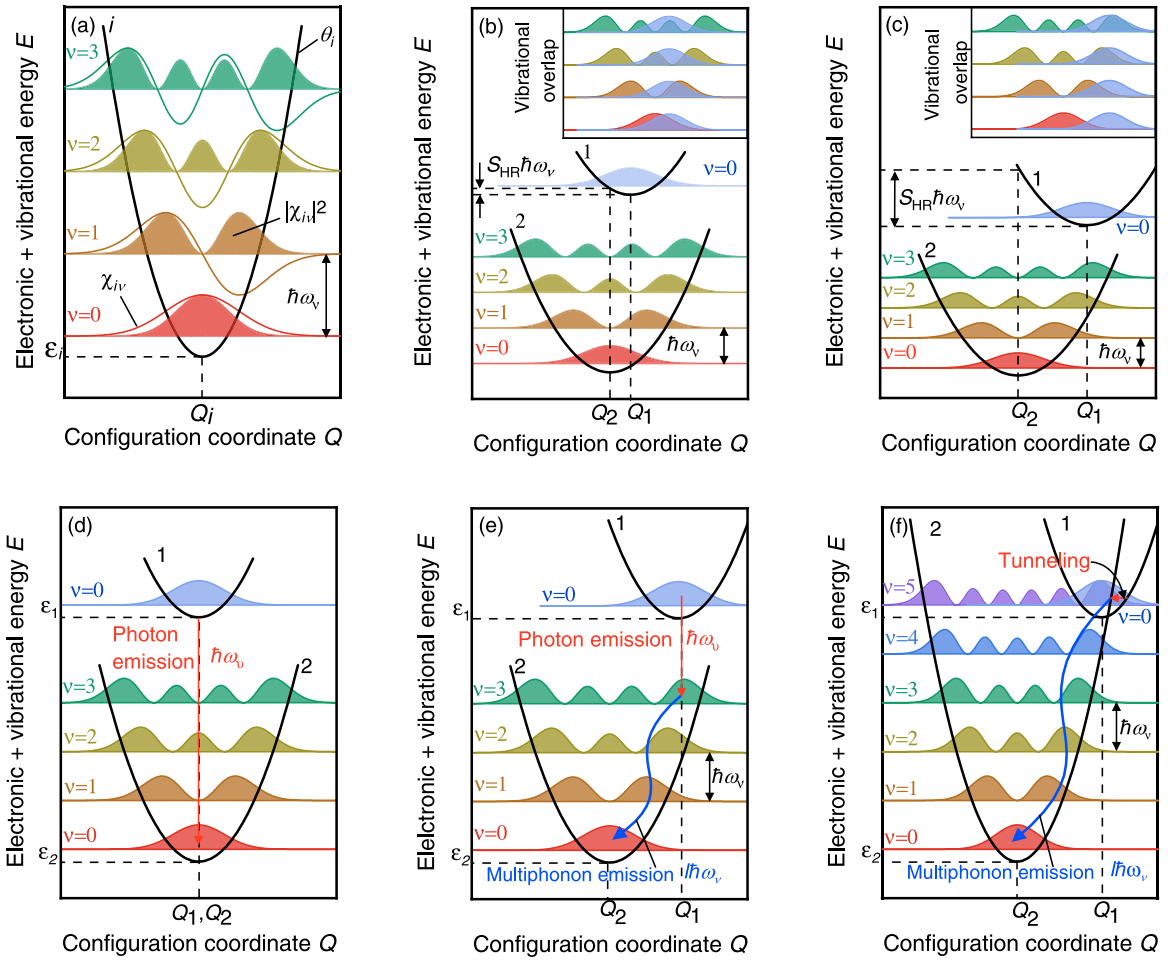

FIG. 3. Configuration coordinate (CC) diagram plots the sum of electronic and vibrational energy of an ith electronic state as a function of some combination of normalized interatomic distances between lattice atoms represented by Q and Q_i gives the equilibrium position of the lattice in the ith state. (a) CC diagram of an ith state. The parabolic curve θ_i represents the energy of a classical harmonic oscillator and superimposed on top of it are the wave functions $\chi_{i\nu}$ of the quantum harmonic oscillator states identified by their vibrational quantum number ν. The absolute square of the wave function $|\chi_{i\nu}|^2$ gives the corresponding probability of finding those states and ε_i gives the electronic energy part of the ith state. $\hbar\omega_\nu$ is the vibration quantum of each vibrational state or the energy of a single phonon. (b) States $|1\rangle$ and $|2\rangle$ are shifted from each other by a small amount resulting in a small Huang-Rhys factor S_{HR} with the inset showing the corresponding overlap between the ground vibrational states of the initial electronic state and vibrational states of the final electronic state. $S_{\mathrm{HR}}\hbar\omega_\nu$ is called the Franck-Condon energy. (c) States $|1\rangle$ and $|2\rangle$ are shifted from each other by a large amount resulting in larger S_{HR} and the inset shows the corresponding vibrational overlaps. (d) Radiative transition between states $|1\rangle$ and $|2\rangle$ in absence of distortions, $\hbar\omega_\upsilon$ giving the energy of the photon emitted in the transition. (e) Radiative capture in the presence of lattice distortions from state $|1\rangle$ by state $|2\rangle$ accompanied by emission of l phonons as the lattice relaxes to equilibrium position. (f) Nonradiative capture via tunneling from state $|1\rangle$ to $|2\rangle$ accompanied by emission of l phonons.

total energy of the system in its ith electronic state is

$$E_i = \varepsilon_i + \tfrac{1}{2}\hbar\omega_i(Q - Q_i)^2, \tag{8}$$

where ε_i is the electronic energy, $\theta_i = \frac{1}{2}\hbar\omega_i(Q - Q_i)^2$ is the vibrational energy of the lattice modeled using a classical harmonic oscillator approximation, and ω_i is the angular frequency of vibration of the lattice atoms about their mean position. In Fig. 3(a), the parabola θ_i gives all possible vibrational energies that a system can have, but from quantum mechanics we know that a vibrating system can only occupy specific vibrational eigenstates of energy $E_{i\nu} = \hbar\omega_i(\nu + 0.5)$ identified by the vibrational quantum number $\nu = 1, 2, 3\ldots$. Superimposing these vibrational wave states on the parabola, evenly spaced in energy ($\hbar\omega_i$ apart from each other), we obtain the complete configurational coordinate diagram, Fig. 3(a), representing the total energy (electronic+vibrational) of the ith electronic state. Here $\hbar\omega_i$ is the vibrational quantum of the electronic state i or the energy of a single phonon. As a result of superposition of the wave picture and the classical picture of vibration, the vibrational wave states extend beyond the classical turning points and are responsible for quantum-mechanical tunneling due to the non-negligible probability of finding the particle beyond the classically allowed region as shown in Fig. 3(a) by the square of the wave function (shaded waves).

In band to band transitions or in the absence of defects the lattice is assumed to be at equilibrium position Q_i and

the vibrational energy part is neglected as the transitions take place between the ground vibrational states of the initial and final electronic state as shown in Fig. 3(d). However, the presence of lattice defects introduces distortions thereby generating strain in the lattice and enhancing the electron-lattice interactions. Microscopically, it means that the equilibrium position of the lattice in the locality of the defect is shifted from equilibrium position elsewhere in the lattice. In such cases, an electron in the ground vibrational state of a conduction band state can transition to a localized defect state both radiatively and nonradiatively as shown in Figs. 3(e) and 3(f), respectively. The vibrational state of the final electronic state for such transition is determined according to the Franck-Condon (FC) [50] principle, which states that the higher the overlap between the initial and final vibrational states, the higher the probability of transition. The extent of this overlap is dependent on the shift in equilibrium position of the two states; the larger the shift, the larger the overlap will be between the initial ground vibrational state and the final excited vibrational state, as shown in the insets of Figs. 3(b) and 3(c). The vibrational energy difference between the minimum of one parabola and the point on it which has the same coordinate Q as the equilibrium position of the other parabola is called the Franck-Condon energy and, assuming that the vibrational frequency of all electronic states are equal, it is expressed as $E_{\mathrm{FC}} = S_{\mathrm{HR}}\hbar\omega_{\upsilon}$ [see Figs. 3(b) and 3(c)], where S_{HR} is the Huang-Rhys factor. The larger the displacement between the minimum of the parabolas, the higher is S_{HR}, and the stronger is the electron-lattice interaction. Symbolically, S_{HR} is expressed as $S_{\mathrm{HR}} = (Q_1 - Q_2)^2/2$ [49]. Now that we have a clear picture of the microscopic transitions, the mathematical forms will be easy to understand.

2. Analytical model of carrier capture

The wave function Ψ_i representing the continuous motion of an electron-lattice system in the ith state is complicated in nature as it describes the motion of the electron with respect to the motion of the lattice. The Born-Oppenheimer (BO) [50] approximation simplifies this problem by considering that an electron transition between two electron energy levels ε_i takes $\sim 10^{-15} - 10^{-16}$ s, whereas lattice vibrations take $\sim 10^{-13} - 10^{-14}$ s to occur [50] and hence, the lattice maintains almost a static position during an electron transition. Thus, the electron wave function ϕ_i of a system in its ith state is defined for a fixed lattice position identified by a fixed value of Q and is a

TABLE II. Equations used in the analytical model of the microscopic theory of radiative and nonradiative carrier capture by defects.

Expressions for quantum defect model that describes the connection between depth of a defect and the radius of the defect wave function [24,49]		
Quantum defect parameter (υ_{T})	$\upsilon_{\mathrm{T}} = \sqrt{R_{\mathrm{H}^*}/\Delta E_{\mathrm{min}}} = \frac{1}{\epsilon_\infty}\sqrt{\frac{m^* q^4}{32\pi^2\hbar^2\Delta E_{\mathrm{min}}}}$	(11)
Radius of the deep defect wave function (R_{T})	$R_{\mathrm{T}} = \frac{a^*_{\mathrm{H}}\upsilon_{\mathrm{T}}}{2}$	(12)
Expressions for calculation of radiative capture coefficients [49]		
Radiative capture coefficient	$k_{\mathrm{n/p}} = \upsilon_{\mathrm{th}}\sum_{E_k}\frac{16}{3}\pi^2\alpha a_{\mathrm{H}}^2\left(\frac{R_{\mathrm{H}}}{\hbar\omega_{\upsilon}}\right)\frac{1}{\eta_{\mathrm{r}}}\frac{M^2_{\mathrm{i,f}}}{2m^*}V\rho_{\upsilon}(\hbar\omega_{\upsilon})J(\hbar\omega_{\upsilon}),$	(13)
Photon density of states	$\rho_{\upsilon}(\hbar\omega_{\upsilon}) = \frac{(\hbar\omega_{\upsilon})^2}{2\pi^2(\hbar\upsilon_{\upsilon})^3}$,	(14)
Radiative transition matrix element	$\lvert M_{\mathrm{i,f}}\rvert^2 = 16\pi m 2^{2\mu} {R_{\mathrm{T}}}^3\left[\frac{\Gamma^2(\mu+1)}{V\Gamma(2\mu+1)}\right]\frac{\sin^2[(\mu+1)\tan^{-1}(\sqrt{E_k/\Delta\mathrm{E}})]}{E_k/\Delta\mathrm{E}(1+E_k/\Delta\mathrm{E})^{\mu+1}}E_k$	(15)
Gamma function [61,62]	$\Gamma(z) = \int_0^\infty e^{-t}t^{z-1}dt$ where $\mathcal{R}(z) \geqslant 0$	(16)
Parameter μ [11]	$\mu = [-\upsilon_{\mathrm{T}}, 0, +\upsilon_{\mathrm{T}}]$, for negative, neutral, and positive defects, respectively.	(17)
Expressions for calculation of nonradiative multiphonon capture coefficients [12,59,60]		
Nonradiative multiphonon capture coefficient	$k_{\mathrm{n/p}} = \frac{M^2_{\mathrm{i,f}}\sqrt{2\pi}}{\hbar^2\omega_{\upsilon}\sqrt{l\sqrt{1+x^2}}}\exp\left\{l\left[\frac{\hbar\omega_{\upsilon}}{2k_{\mathrm{B}}T} + \sqrt{1+x^2} - x\cosh\left(\frac{\hbar\omega_{\upsilon}}{2k_{\mathrm{B}}T}\right)\right.\right.$ $\left.\left. - \ln\left(\frac{1+\sqrt{1+x^2}}{x}\right)\right]\right\}$	(18)
No. of phonons emitted during multiphonon transition	$l = \frac{\Delta E}{\hbar\omega_{\upsilon}}$	(19)
Multiphonon transition matrix element	$\lvert M_{\mathrm{i,f}}\rvert^2 = V_{\mathrm{T}}(l\hbar\omega_{\upsilon})^2$	(20)
Volume of the defect V_{T}	$V_{\mathrm{T}} = \frac{4}{3}(\pi R_{\mathrm{T}})^3$	
Parameter x	$x = \begin{cases} \frac{S_{\mathrm{HR}}}{l\sinh(\hbar\omega_{\upsilon}/2k_{\mathrm{B}}T)} & \text{for } S_{\mathrm{HR}} < l \\ \frac{l}{S_{\mathrm{HR}}\sinh(\hbar\omega_{\upsilon}/2k_{\mathrm{B}}T)} & \text{for } S_{\mathrm{HR}} > l \end{cases}$	(21)
Expressions for calculation of Huang-Rhys factor [11]		
Huang-Rhys factor for polar optical coupling	$S_{\mathrm{HR}} = \frac{3}{2(\hbar\omega_{\upsilon})^2}\left[\frac{q^2\hbar\omega_{\upsilon}}{a_0^3 q_{\mathrm{D}}^2}\left(\frac{1}{\epsilon_\infty} - \frac{1}{\epsilon}\right)\right]I\left(-2, 2\mu, \frac{q_{\mathrm{D}}a^*_{\mathrm{H}}\upsilon_{\mathrm{T}}}{2}\right)$	(22)
Huang-Rhys factor for optical deformation potential coupling	$S_{\mathrm{HR}} = \frac{1}{2(\hbar\omega_{\upsilon})^2}\frac{\hbar D^2}{M_{\mathrm{r}}\omega_{\upsilon}}I\left(0, 2\mu, \frac{q_{\mathrm{D}}a^*_{\mathrm{H}}\upsilon_{\mathrm{T}}}{2}\right)$	(23)
Function I	$I(a, b, c) = \frac{1}{(bc)^2}\int_0^1\frac{y^a\sin^2[b\tan^{-1}(cy)]}{[1+(cy)^2]^b}dy$	(24)

TABLE III. Expressions and values of material parameters used in the simulation.

Parameter	Symbols or expressions	MAPI	GaAs	Si
Trap energy	E_T	Variable	Variable	Variable
Trap depth	ΔE	Variable	Variable	Variable
Distance from the nearest band	ΔE_{min}	Variable	Variable	Variable
Thermal velocity	v_{th}	1×10^7 cm/s	1×10^7 cm/s	1×10^7 cm/s
Phonon energy	$\hbar\omega_v$	16.5 eV	30 eV	55 eV
Photon energy	$\hbar\omega_v$	Variable	Variable	Variable
Permittivity	$\epsilon(f)$	$\epsilon_\infty = 5\epsilon_0$ [63]	$\epsilon_\infty = 10.9\epsilon_0$ [49]	$\epsilon_\infty = 11.9\epsilon_0$ [49]
$\epsilon_0 = 8.85 \times 10^{-12}$ F/m		$\epsilon = 33.5\epsilon_0$	$\epsilon = 13.18\epsilon_0$	$\epsilon = 11.9\epsilon_0$
Refractive index	$\eta_r = \sqrt{\epsilon_\infty/\epsilon_0}$	2.23	3.30	3.44
Pekar factor	$(\epsilon_\infty^{-1} - \epsilon^{-1})$	1.92×10^{10} F/m	1.79×10^9 F/m	0
Lattice constant	a_0	6.3 Å [63]	$\sqrt[3]{(1/4)} \times$ 5.6 Å [49]	$\sqrt[3]{(1/4)} \times$ 5.4 Å [49]
Radius of sphere of the Brillouin zone	$q_D = \sqrt[3]{6\pi^2}/a_0$	6.18 nm^{-1}	11.04 nm^{-1}	11.45 nm^{-1}
Effective mass	m^*	0.2	0.082	0.2
Reduced mass	M_r	78.7 amu	36.11 amu	28 amu
Fine-structure constant	$\alpha = q^2/4\pi\epsilon_0\hbar c$	1/137	1/137	1/137
Bohr radius	$a_H = 4\pi\epsilon_0/mq^2$	5.292×10^{-2} nm	5.292×10^{-2} nm	5.292×10^{-2} nm
Effective Bohr radius	$a_H^* = a_H\epsilon/m^*$	8.86 nm	8.05 nm	3.15 nm
Rydberg energy	$R_H = q^2/(8\pi\epsilon_0 a_H)$	13.605 eV	13.605 eV	13.605 eV
Effective Rydberg energy	$R_H^* = q^2/(8\pi\epsilon a_H^*)$	2.4 meV	6.4 meV	19.2 meV
Sommerfeld factor	$s_a = 4(\pi R_H^*/k_B T)$	2.17	3.53	6.11

function of the electron coordinate $\vec{r}$ only. The ith electronic state lattice wave function χ_{iv} is a function of Q and identified by $v = 1, 2, 3....$ Thus, the system wave function in terms of BO states [51] is

$$\Psi_i(r, Q) = \phi_i(r, \mathrm{Q})\chi_{iv}(Q). \tag{9}$$

Using this form of wave functions in Eq. (6) and applying the FC principle simplifies the transition probability to

$$M_{1,2} = \underbrace{\langle\phi_1|\hat{H}_{int}|\phi_2\rangle}_{\text{transition element}} \underbrace{\langle\chi_{1v}|\chi_{2v}\rangle}_{\text{overlap factor}}. \tag{10}$$

The FC principle [50] lets us simplify the total matrix element as a product of the electron transition matrix element, which is independent of the lattice coordinate Q (it is calculated for a fixed value of Q), and the Q-dependent overlap factor. This simplification, known as the Condon approach, greatly reduces the complications of the analytical calculation and has been extensively used in the calculation of both radiative and nonradiative multiphonon calculations [6,7,23,24]. However, some other approaches [7,10,11,51–57] exist and a brief discussion about them is presented in Sec. I of the Supplemental Material [58].

However different the approaches may be, they use the quantum defect model [23,49] of wave functions based on the effective-mass approximation to model a defect state. The quantum defect model is characterized by a quantum defect parameter v_T (see Table II for expressions) which ensures that the deeper the defect, the more diminished the radius of the defect wave function R_T and hence more localized it is. Within the purview of the effective-mass approximation, a shallow trap in a material is characterized by a binding energy given by the effective Rydberg energy $R_H{}^*$ (see Table III for expression and value) and a radius given by the effective Bohr radius $a_H{}^*$ of the material. As a defect in the material gets deeper, the radius shrinks from its original value as a function of the depth of the defect from the nearest band given by ΔE_{min}. The dimensionless quantity v_T represents the proportionality factor that relates the change in binding energy of the defect to a change in the radius of the defect wave function. The factor is expressed as the square root of the ratio between the binding energy of a shallow trap in a material and the actual depth of the deep defect in the same material.

Once the electronic wave functions describing the band state, the defect state, and the lattice wave functions representing the lattice vibrations are defined, the next logical step is the calculation of the matrix element $M_{i,f}$ giving the probability of electron transition between a defect state and a band state. The stronger the interaction between the defect and the band state, the higher the probability of electron transition between the initial and final states. Besides the electron transition element, the overlap between the initial and the final vibrational state will also affect the probability of transition. In the case of negligible lattice distortion, the vibrational ground states of the initial and final electronic states completely overlap each other giving an overlap factor of approximately 1 and the transition probability is at its maximum. The capture coefficients $k_{n/p}$ can be readily obtained once we have the right matrix elements. The analytical forms of the capture coefficients are listed in Table II. Table III gives the equations and actual values of all the parameters used in the analytical modeling.

The model for the nonradiative multiphonon capture process has been adapted from the works of Markvart [12,59].

The model calculates the multiphonon capture coefficients from the tunneling rate between the two parabolas using Wentzel-Kramers-Brillouin approximation and is valid for all temperature ranges. However, the electron transition matrix element is taken from Ridley [49]. The multiphonon transition of a carrier to a defect is from either of the two band edges with simultaneous emission of l phonons each of energy $\hbar\omega_\nu$. In this case the depth of the defect $\Delta E = l\hbar\omega_\nu$. The detailed discussion can be found in a previous publication [60] and the final equations are given in Table II.

The model to obtain radiative capture coefficients has been adapted from the theory presented by Ridley [49] (see Table II for analytical expressions). For simplicity we assume that the presence of the defects introduces negligible distortions in the lattice and that the initial and final-state vibrational wave functions overlap each other giving an overlap factor $J(\hbar\omega_\nu) = 1$ [24,49]. Under this assumption, the radiative capture coefficient is independent of S_{HR} as well as phonon energy $\hbar\omega_\nu$ since the capture takes place purely radiatively by emission of a photon of energy $\hbar\omega_\upsilon = \Delta E + E_k$. In contrast to the nonradiative multiphonon scenario where only the transitions between either band edge and defects are considered, in the radiative capture processes transitions to a defect state E_{T} from all kth band states with energy E_k within $3k_{\mathrm{B}}T$ of the band edge are considered since $\hbar\omega_\upsilon \gg 3k_{\mathrm{B}}\mathrm{T}$. Details of the radiative capture model are given in Sec. II of the Supplemental Material [58].

The charge state of the defect impacts the defect wave function and the effect is included by multiplying the quantum defect parameter υ_{T} by charge $\pm Ze$ carried by the defect to give a parameter μ. Coulomb attraction between oppositely charged carriers and defect states carrying a charge $\pm Ze$ also enhances the speed of capture and to include this effect we multiply the k_{n} of a donor defect and the k_{p} of an acceptor state with a Sommerfeld factor s_{a}.

As mentioned earlier and as is evident from the expressions for capture coefficients given in Table II, the capture coefficients depend on S_{HR} and S_{HR} in turn depends on the displaced equilibrium position of the lattice in the vicinity of the defect. These displacements are the key to an understanding of the multiphonon process. Microscopically, such displacements can be due to the presence of polar optical phonons, which indicates an out-of-phase motion of the lattice atoms causing polarization effects in the lattice. The interaction of the carriers with the Coulomb field of the polarized lattice waves is called polar optical coupling. Also due to this out-of-phase motion, variations identified as optical deformation potential D (eV/cm) are introduced in the band energy levels and electron interactions with such variations are called optical deformation potential interaction. Ridley [11] gave analytical forms of the S_{HR} for both polar optical coupling and optical deformation potential coupling. The expression of S_{HR} for polar optical coupling (given in Table II) reveals a strong dependence on the Pekar factor $(\epsilon_\infty^{-1} - \epsilon^{-1})$. This dependence suggests that larger differences between the high- and low-frequency permittivity cause an increase in S_{HR} and hence in the electron-lattice interaction. However, the S_{HR} due to optical deformation potential is proportional to D^2. The dominant mode of electron-lattice coupling for multiphonon emission is determined by the higher of two values of S_{HR}. In polar

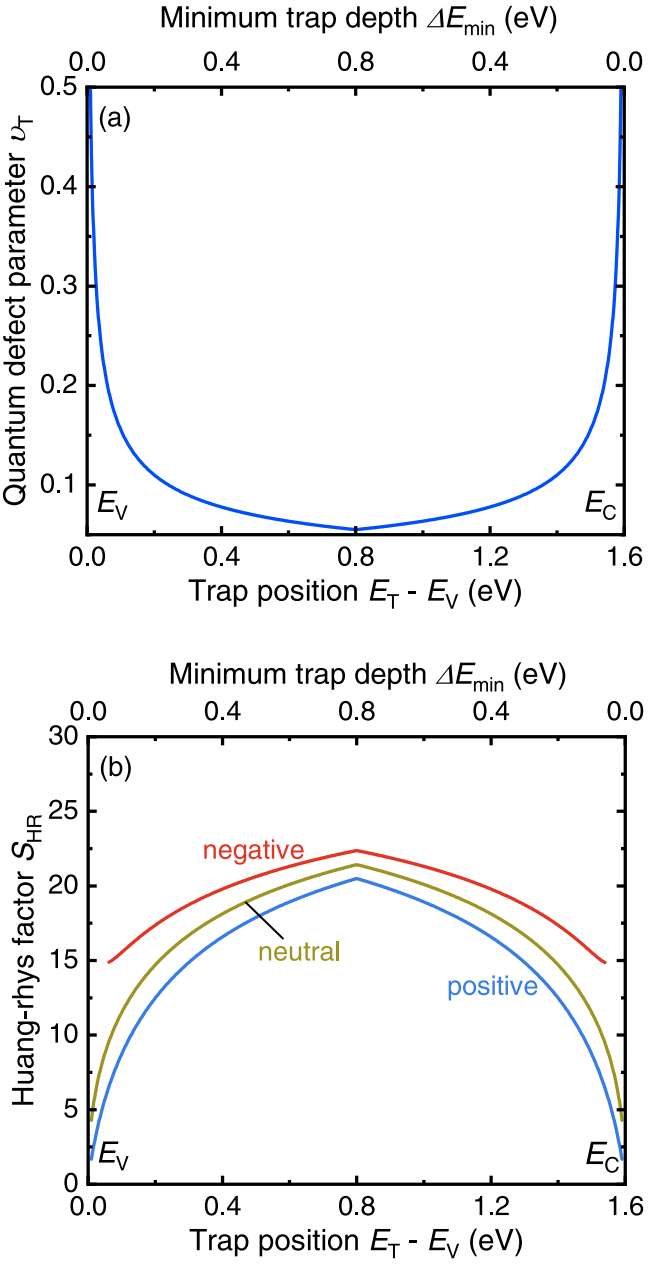

FIG. 4. The variation of quantum defect parameter and Huang-Rhys factor with trap position in MAPI. (a) Quantum defect parameter υ_{T} is plotted as a function of trap position $E_{\mathrm{T}} - E_{\mathrm{V}}$. (b) Huang-Rhys factor S_{HR} calculated using υ_{T} is shown as a function of trap position. The S_{HR} is maximum when the defect is farthest from both the bands, i.e., at the midgap where ΔE_{min} is maximum. The higher the S_{HR} the stronger is the interaction between the electrons and the lattice.

semiconductors, such as MAPI, lattice polarization is strong given the high Pekar factor and thus polar optical coupling is dominant. This contrasts with GaAs which has a low Pekar factor and hence optical deformation potential coupling dominates. For Si, which is a covalent semiconductor, the Pekar factor is 0 and the electron-lattice interaction is modeled in deformation potential approximation [59].

After we have collected all the necessary formulas for calculating the capture coefficients in the harmonic

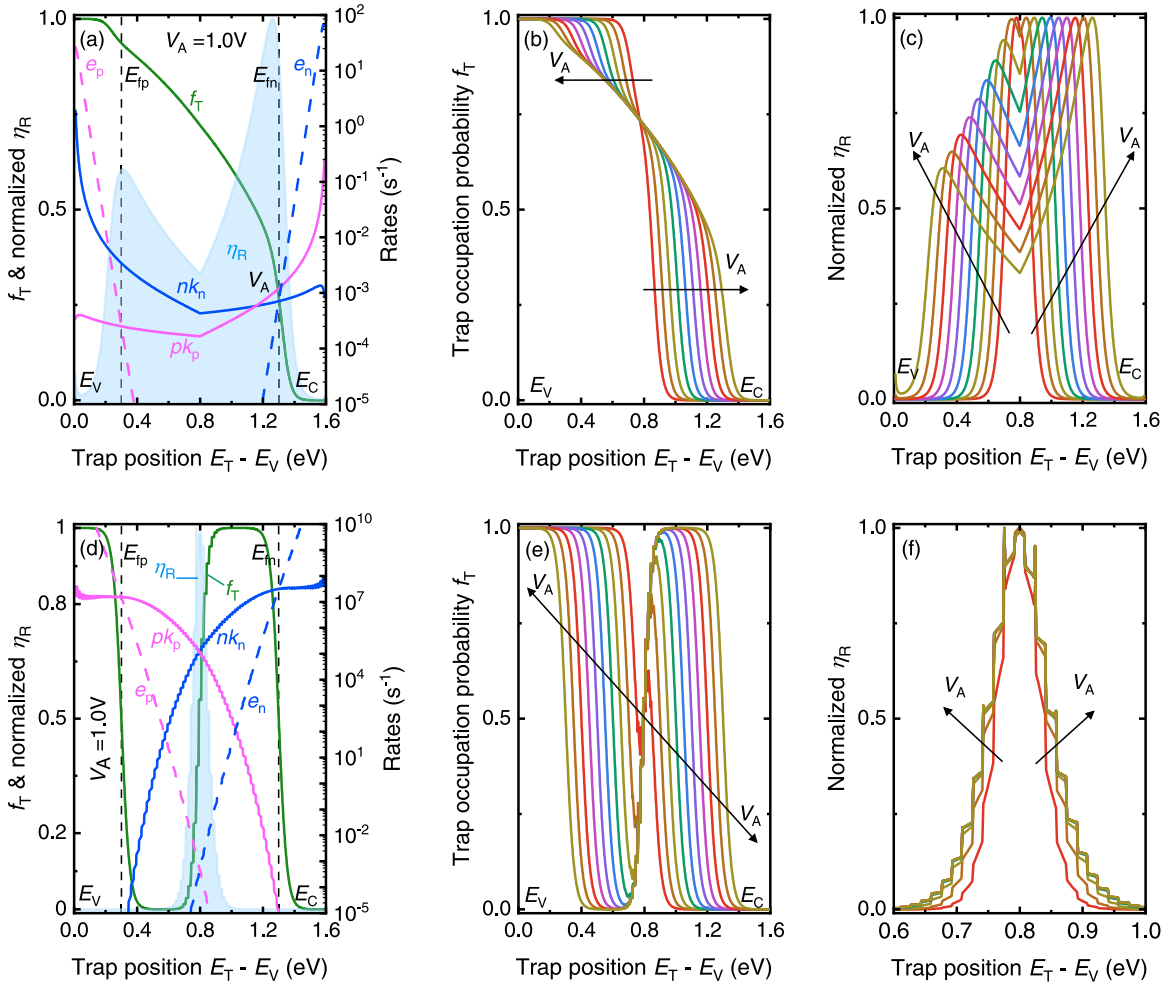

FIG. 5. Trap occupation probability f_T and normalized recombination efficiency η_R is obtained from trap position dependent capture and emission rates of MAPI. (a) Radiative capture rates, emission rates, and the corresponding f_T and η_R is given as a function of trap position $E_T - E_V$ at an applied voltage $V_A = 1.0$ V. (b) Trap occupation probability f_T due to radiative capture and emission as a function of trap position for varying applied voltage $V_A = 0.1$–1.0 V. (c) Normalized η_R due to radiative capture and emission as a function of $E_T - E_V$ for $V_A = 0.1$–1.0 V. (d) Multiphonon capture, emission rates, and the corresponding f_T and η_R is given at an applied voltage $V_A = 1.0$ V. (e) f_T due to multiphonon capture and emission as a function of trap position for $V_A = 0.1$–1.0 V. (f) Normalized η_R due to multiphonon capture and emission as a function of trap position for $V_A = 0.1$–1.0 V. The x axis has been expanded to show only the relevant energy range. In a real device the capture process is dominated by the multiphonon relaxation as is evident from the absolute value of the coefficients indicated on the right y axis of panels (a) and (d). So f_T and normalized η_R for a combined case is identical to panels (e) and (f).

approximation, we can proceed to study their behavior as a function of the defect position $E_T - E_V$ and its effect on the recombination statistics.

III. RESULTS

The capture coefficients are the key parameters we extract from the microscopic model. These coefficients are then used as input to the statistical model to understand the effect of the recombination kinetics on the recombination statistics. In the microscopic model of carrier capture we noticed that the capture coefficients are functions of the defect localization as the Huang-Rhys factor S_{HR} is itself a function of the quantum defect factor υ_T. So, following a bottom-up approach we start by plotting the trap position dependence of υ_T and S_{HR} in Figs. 4(a) and 4(b), respectively, using the parameters of MAPI as an example. In Fig. 4(a), υ_T diminishes and thus the defect becomes more localized as the defect moves further away from either band and is minimum at the middle of the band gap where ΔE_{min} is maximum. A localized defect leads to strong electron-lattice interaction and the Huang-Rhys factor increases as a result as illustrated in Fig. 4(b). All three defect centers become more confined as a function of ΔE_{min}. (See Sec. III of the Supplemental Material for more information on the validity of the model [58].) The parameter μ expressing the charge state of the defect greatly influences the relative magnitude of S_{HR} by varying the power term in the denominator of $I(a, b, c)$ given by Eq. (24) of Table II. The S_{HR} of the negatively charged states is maximum, indicating the strongest electron-lattice interaction as can be seen in Fig. 4(b).

In Fig. 5 we use the material parameters of MAPI and the S_{HR} obtained in Fig. 4(b) to study the effect of the capture rates on the trap occupation probability and recombination

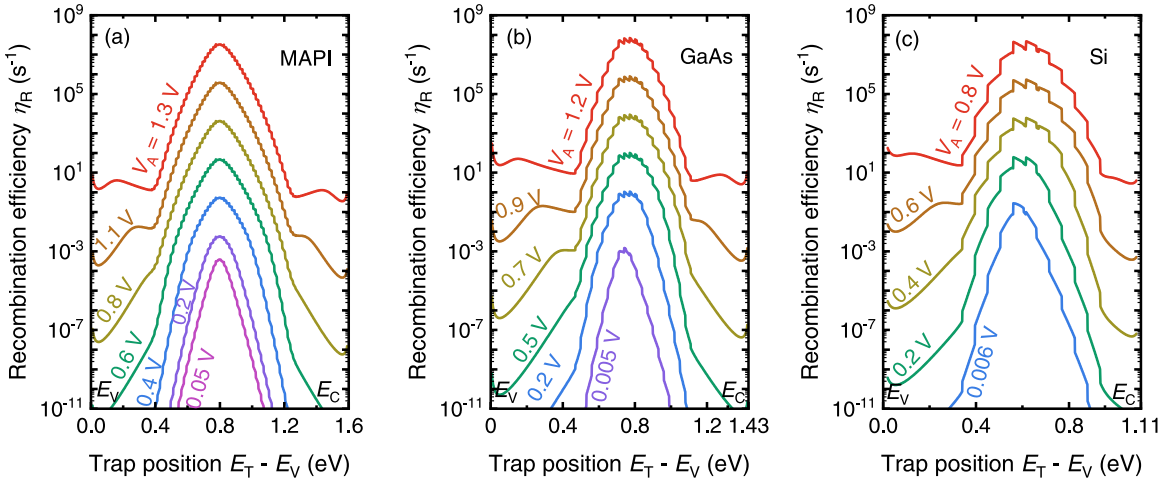

FIG. 6. The absolute value of recombination efficiency η_R is plotted using the parameters for MAPI, GaAs, and Si for various values of applied voltage V_A. Assuming a trap density $N_T = 10^{15}/cm^3$ and $n = p$. (a) Recombination efficiency η_R as a function of trap position $E_T - E_V$ in MAPI for polar optical electron-lattice coupling. (b) Recombination efficiency η_R as a function of trap position $E_T - E_V$ in GaAs for an optical deformation potential $D = 10^9$ eV/cm. (c) Recombination efficiency η_R as a function of trap position $E_T - E_V$ in Si for an optical deformation potential $D = 10^9$ eV/cm. The increasing asymmetric behavior noted in the three plots is due to the multiplication of the Sommerfeld factor with the electron capture rates by positively charged donor states. The Sommerfeld factor increases from MAPI to GaAs and finally to Si.

efficiency. Capture rates are plotted to maintain dimensional consistency with emission coefficients which are equivalent to emission rates. The trends of capture coefficients and capture rates are similar and a figure showing the actual values of capture coefficients for both radiative and multiphonon capture has been included in Sec. IV of the Supplemental Material [58]. When the defect level occurs near the band edges, the captured carriers are very easily thermally excited back to their respective bands and the capture rates are much slower in comparison to the corresponding thermal emission rates as shown in Figs. 5(a) and 5(d). This results in $f_T \sim 1$ when $E_V < E_T - E_V < E_{fp}$ (high hole emission) and $(1 - f_T) \sim 1$ when $E_{fn} < E_T - E_V < E_C$ (high electron emission) and negligible recombination, i.e., $\eta_R \approx 0$ as shown in Figs. 5(a), 5(c), 5(d), and 5(f). However, when the defect levels are within the two quasi-Fermi levels, the emission rates are smaller in comparison to the capture rates and the defect levels act as recombination centers. The recombination efficiency η_R is given by the slower of the two capture coefficients and $f_T > 0.5$ when $nk_n > pk_p$ and $f_T < 0.5$ when $nk_n < pk_p$.

In a real MAPI absorber layer the carriers are more likely to be captured by defects through multiple phonon emission processes as in comparison to the multiphonon capture rates [right y axis of Fig. 5(d)], the radiative capture rates [right y axis of Fig. 5(a)] are negligible. However, unless the defect level is around midgap energy, one of the capture rates is substantially smaller than the other and will slow down the recombination process. According to the model developed here based on harmonic oscillator approximation, the defect is most detrimental only when it is present at the absolute center of the band gap. But in MAPI, due to relatively high formation energy, defect densities are low at midgap [26]. This suggests that most defects present are not highly recombination active, making MAPI less susceptible to loss of carriers through recombination. The results discussed here are for donorlike defects and the results for acceptorlike defects given in Sec. V of the Supplemental Material show similar trends. The effect of the charge state on S_{HR}, Fig. 4(b), influences the magnitude of capture rates also. Please see Sec. V of the Supplemental Material [58] for further discussion on the effect of defect charge states on capture rates.

So far, we have considered the effects of the polar optical coupling only, it being the dominant mechanism of electron-lattice coupling in MAPI. The dominant coupling mechanism in GaAs and Si is optical deformation potential and we assume $D = 10^9$ eV/cm [see Fig. 8(a)] to plot η_R in GaAs and Si as a function of trap position in Figs. 6(b) and 6(c), respectively, for various values of V_A. Then we compare the two plots with Fig. 6(a) which gives η_R for polar optical coupling in MAPI. The recombination efficiencies predicted by this harmonic oscillator model, assuming $N_T = 10^{15}/cm^3$ and a high injection scenario such that $n = p$, exhibit similar trends in all three materials. Figure 6 contradicts the popular idea that all defects between the two quasi-Fermi levels are equally recombination active and shows that it is only the midgap defects that contribute to the highest recombination efficiency or the lowest SRH lifetime τ_{eff} irrespective of the material or the type of electron-phonon coupling. Given the change in band gap between the three materials, comparing the data at equal voltage would not be a fair comparison because it would correspond to strongly different carrier concentrations. Therefore, we take the open-circuit voltage in the Shockley-Queisser model for each of the three materials and then use this voltage as the maximum voltage. Other voltages are chosen to correspond to a certain luminescence quantum efficiency Q_e^{lum}. Given that any order of magnitude in luminescence quantum efficiency leads to a loss of $k_B T/q \times \ln(10)$ in open-circuit voltage (relative to the radiative limit), lines [44] of equal color now correspond to open-circuit situations with identical luminescence quantum efficiency.

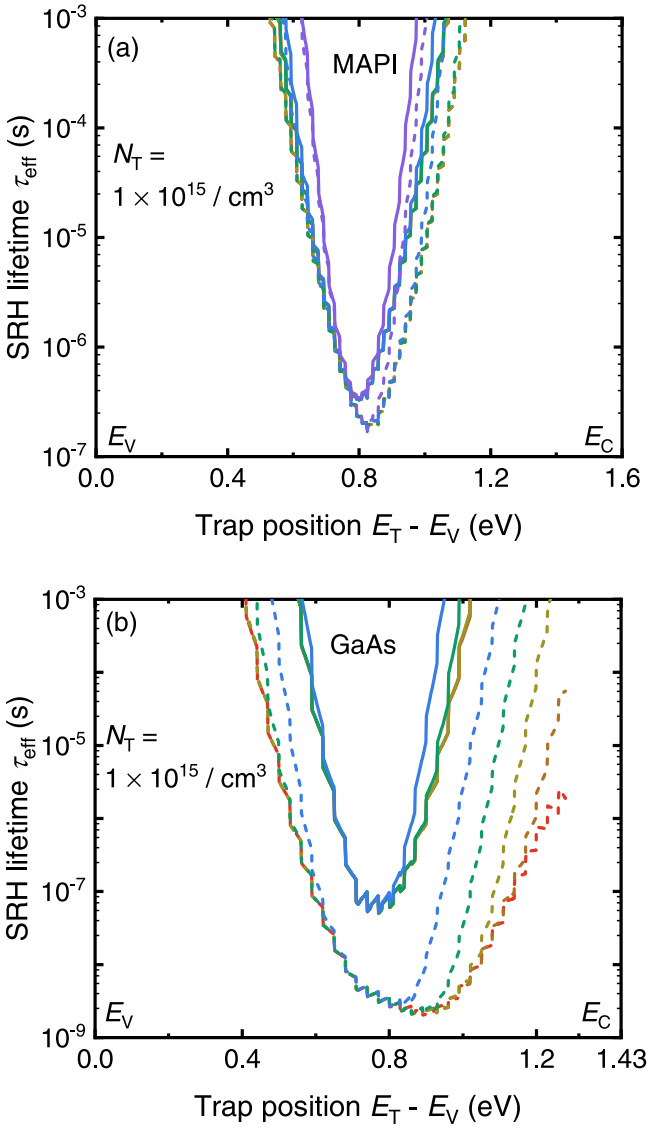

FIG. 7. The SRH lifetime τ_{eff} is plotted as a function of defect position for a trap in MAPI and GaAs when the trap density $N_T = 10^{15}/\text{cm}^3$ and a high injection of carriers leads to $n = p$. The solid lines represent donorlike defect states, whereas the dashed lines represent acceptorlike defect states. (a) In MAPI, the acceptorlike and the donorlike defects give almost identical SRH lifetimes. (b) In GaAs, the acceptorlike and donorlike midgap defects show considerable difference in the lifetime with the acceptorlike midgap defects contributing to faster recombination.

In Figs. 7(a) and 7(b) we compare the SRH lifetimes of MAPI and GaAs for both donorlike as well as acceptorlike defects for a trap density $N_T = 10^{15}/\text{cm}^3$. Figure 7(a) shows that, when $n = p$, irrespective of the possible charge configuration of the defect, for an assumed trap density of $N_T = 10^{15}/\text{cm}^3$ in MAPI, a SRH lifetime of about $\tau_{eff} \leqslant 10^{-5}$ s is primarily contributed by the defects which are positioned within a narrow range of 20 meV on either side of the midgap energy ($0.6\,\text{eV} < E_T - E_V < 1.0\,\text{eV}$). This is because the high effective mass, high low-frequency permittivity, and low phonon energy in MAPI leads to comparable capture rates in acceptorlike and donorlike defects. (See the discussion on the effect of defect charge states on capture rates in Sec. V of the Supplemental Material [58].) In addition, the interplay of these material parameters also ensures very symmetric and exponentially decaying capture rates as shown in Fig. 5(d), making only the defects around the midgap energy recombination active and contributing to relevant SRH lifetimes. However, defect levels in MAPI determined both experimentally and using density functional theory by various authors (summarized very well in Ref. [26]) show that most defect levels are not situated within the 20 meV range on either side of the midgap energy, i.e., they are mostly outside the energy range of ($0.6\,\text{eV} < E_T - E_V < 1.0\,\text{eV}$). The fairly low density of defects in this energy range in MAPI indicates that most of the nonradiative recombination of carriers happens at defect levels occurring outside the ($0.6\,\text{eV} < E_T - E_V < 1.0\,\text{eV}$) range where the SRH lifetimes are longer, $\tau_{eff} > 10^{-5}$ s, thus leading to a slower nonradiative recombination mechanism and longer nonradiative lifetimes which is crucial for enabling high efficiencies. The findings in MAPI are in contrast with GaAs, as illustrated in Fig. 7(b), in which even when $n = p$ and at trap density of $N_T = 10^{15}/\text{cm}^3$, recombination lifetimes of the acceptorlike defects are much shorter compared to the donorlike defects. Fe, Cr, and Cu, which are well-known acceptor defect levels in GaAs [9], therefore contribute to shorter SRH lifetimes even though being 20–50 meV away from the midgap energy.

In Fig. 8 we compare the Huang-Rhys factor of GaAs obtained from the analytical model presented here to that reported by Henry and Lang for GaAs [9] in order to study the validity of the model. Since the absolute value of the optical deformation potential D is not known, we assume Eqs. (13) and (18) presented in Table II to correctly represent the physical processes and reproduce the experimental data presented by Henry and Lang for GaAs [9] by using D as the fitting parameter. In contrast to the usual notion of a constant D for all trap states, a strong dependence of D on trap position as well as the charge state of the defect is noticed in Fig. 8(a). The D values so obtained are then used to obtain S_{HR} values of neutral and negatively charged acceptorlike states, which are plotted in Figs. 8(b) and 8(c), respectively. Then, for comparison, we plot S_{HR} theoretically calculated using Eq. (14) for neutral and negative charge states of acceptorlike defects at $D = 5 \times 10^8\,\text{eV/cm}$, $7 \times 10^8\,\text{eV/cm}$, and $10^9\,\text{eV/cm}$. The agreement in the trends of theoretical and experimental plots ensures the validity of the model used. The Huang-Rhys factor increases as the trap gets away from either of the band edge or ΔE_{min} increases. However, the difference between the theoretical and experimental values of S_{HR} is due to the constant D values that go into the theoretical calculation. More robust ways to determine trap position dependent D values are necessary to eliminate such differences.

In Fig. 9, we use the same data fitting method to study the temperature dependence of D and conclude that it is weak. The purpose of this study is to ensure that the temperature dependence of the capture cross section presented by Henry and Lang [9] is not due to temperature dependence of the deformation potential but most likely due to the temperature dependent nature of defect localization. Unfortunately, within the realm of the quantum defect model of defect wave

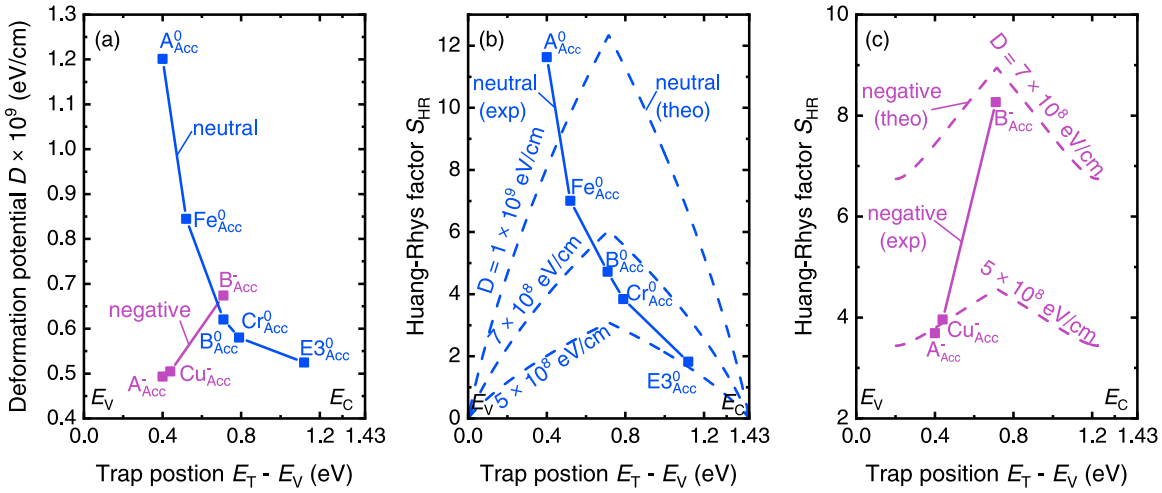

FIG. 8. Trap position dependence of optical deformation potential D and Huang-Rhys factor S_{HR} in GaAs. (a) D values for neutral and negative acceptor states obtained from the experimental curves of electron and hole capture cross sections, respectively, at $T = 300$ K given by Henry and Lang for GaAs in Ref. [9] as a function of trap position. (b) The solid curve shows the Huang-Rhys factors calculated using the D values determined for neutral acceptor state in panel (a). The dashed curves show the theoretical values of S_{HR} for neutral charge states at fixed D values. (c) The solid curve shows the Huang-Rhys factors of a negatively charged acceptor state calculated using corresponding D values in panel (a). The dashed curves show the theoretical values of S_{HR} for negative charge states at fixed D values.

function, there is no way to treat the temperature dependence of defect localization.

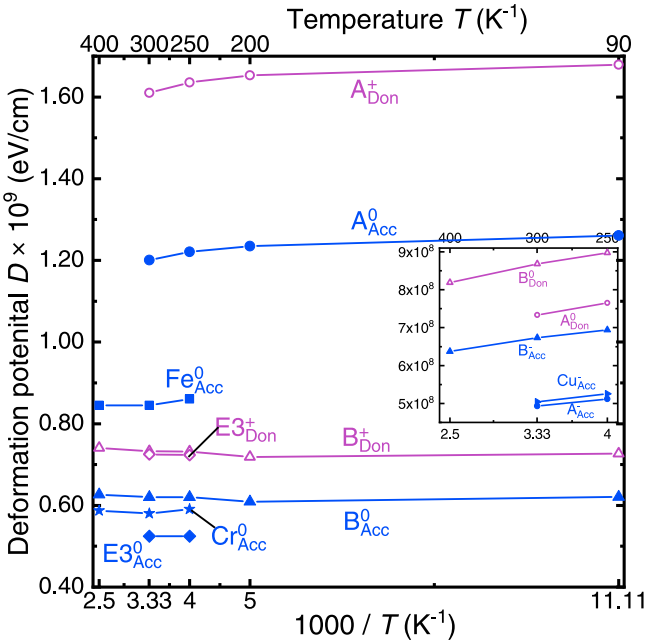

FIG. 9. The optical deformation potential D as a function of temperature T in GaAs is studied. The D values are obtained from data fitting of the experimental electron capture cross-section data given by Henry and Lang for GaAs in Ref. [9]. The open symbols represent donor states, whereas the filled symbols represent acceptor states. Fe, Cr, and Cu are well-known acceptor centers and thus the fitted data has only accounted for charge configurations of acceptor defect. Center A, B, and E3 could be either acceptors or donors and thus plots show both charge states for such defect centers. The inset gives the D values for hole capture cross section.

IV. CONCLUSION

The efficient conversion of incoming photon energy into electrical energy relies not only on the efficient absorption of the photons but also on limited conversion of the electrical energy into thermal energy by means of nonradiative transitions. Material defects contribute to the nonradiative recombination mechanisms by acting as an alternative path of escape for the excited electrons from the conduction band to the valence band. However, not all defects are equally effective in acting as a recombination center and the purpose of the current study is to give a better overview about which defects are the most detrimental for device performance or deep defects.

From a mechanistic point of view, a deep defect is a defect that substantially accelerates recombination. In the framework of SRH statistics, the recombination efficiency is the quantity that defines the connection between the relative rate of recombination and the depth of a defect. Hence, one could argue that a deep defect is a defect with an energy level, where the normalized recombination efficiency is close to 1. A more general statement would be that the recombination efficiency is high whenever the occupation of a defect is approximately ½ (i.e., it is half full), which is equivalent to saying that the rate of electrons being captured by the trap is equal to the rate at which holes are captured by the trap. At the same time emission of electrons from the trap back into the conduction band and holes back into the valence band need to be small relative to the respective inverse processes of capture. Thus, a deep defect is one that fulfills the criteria $nk_n = pk_p$ and $nk_n \gg e_n$ and $pk_p \gg e_p$. For a specific defect in a specific material, one would now have to calculate the rates of capture and emission to see whether they fulfill the above-mentioned criteria. Previously, the recombination efficiency of defects in the framework of the SRH statistics has only been calculated using constant capture coefficients [5,41] leading to the result that deep defects are those defects that lie in between the

two quasi-Fermi levels [see Fig. 2(e)]. For typical working conditions of solar cells, the quasi-Fermi levels are split by several hundreds of meV at the maximum power point, which would imply that defects within a large range of depths within the band gap could be deep defects. Here, we argue that this concept largely overestimates the energetic width of the recombination efficiency. We also attempt to make a generic statement about recombination activity of defects in different materials by making use of the theory of optical and multiphonon transitions in the harmonic oscillator approximation. In this case, one arrives at a substantially different result. Given that the rate coefficients for multiphonon transitions are strongly dependent on the energetic distance between the states (and therefore the depth of the trap), only a very small range of energies will allow the condition $nk_n = pk_p$ to be approximately true. This implies that the adjective "deep" has to be understood as defining a rather narrow range of energies of only tens of meV at which the harmonic oscillator model would predict defects to be most detrimental for recombination. Defects outside of this narrow range of energies could still be efficient at capturing one type of charge carriers but not of both types of charge carriers.

We also note that the harmonic oscillator model has limitations and should not be considered as being universally valid. The defect wave function defined within the realms of the quantum defect model is based on the effective mass and the electrical permittivity of the absorber material and distinguishes one defect center from another based on the energetic depth of the defect only and not based on the elemental mass or any other chemical properties of the defect center. This simplified model of the defect center circumvents the complexities arising in real materials and gives us important insights about defect-mediated recombination, but it fails to show how the nature of defect centers influences the capture coefficients. Also, the lattice vibrations modeled in a harmonic approximation cannot treat the occurrence of anharmonicity in the potential energy surfaces of the electron-lattice system at crossovers, i.e., when the lattice vibrations are very strong, and the lattice displacements are very large. In addition, the band state wave functions are modeled using an effective-mass approximation and a parabolic energy dispersion relationship is considered for the conduction and valence band, which clearly cannot include the effect of nonparabolicity in the bands of real materials. To deal with all such shortcomings of the general theory outlined above, material-specific atomistic modeling of absorber materials and defect centers is necessary as already presented in [35–38,64–67]. However, since such calculations are computationally expensive and are usually done for specific defect centers, device simulation to study the rates of recombination with the capture coefficients will be limited to specific traps. In contrast, the generic model we present is a lot more flexible regarding the position of the trap and is useful for estimating the effect of defects in situations, where no calculations of the potential energy surface of defects are available yet. The calculated capture rates could be important for general solar-cell device simulation [32,33,46–48], material screening [40–42] modeling of experimental methods that are affected by defect-assisted recombination (such as photoluminescence) [29], and for estimating the effect of defects on device performance [30].

ACKNOWLEDGMENTS

B.D. acknowledges the HITEC graduate school at Forschungszentrum Jülich for support from a PhD fellowship. I.A. acknowledges funding from the European Commission Horizon 2020 project No. 824158 ("EoCoE-II"). T.K. acknowledges the Helmholtz Association for funding via the PEROSEED project.

[1] C. T. Sah and W. Shockley, Phys. Rev. **109**, 1103 (1958).
[2] C. T. Sah, R. N. Noyce, and W. Shockley, Proc. IRE **45**, 1228 (1957).
[3] W. Shockley and W. T. Read, Phys. Rev. **87**, 835 (1952).
[4] R. N. Hall, Phys. Rev. **87**, 387 (1952).
[5] J. G. Simmons and G. W. Taylor, Phys. Rev. B **4**, 502 (1971).
[6] K. Huang and A. Rhys, Proc. R. Soc. London, Ser. A **204**, 406 (1950).
[7] R. Kubo and Y. Toyozawa, Prog. Theor. Phys. **13**, 160 (1955).
[8] H. Gummel, and M. Lax, Ann. Phys. **2**, 28 (1957).
[9] C. H. Henry and D. V Lang, Phys. Rev. B **15**, 989 (1977).
[10] B. K. Ridley, J. Phys. C: Solid State Phys. **11**, 2323 (1978).
[11] B. K. Ridley, Solid State Electron. **21**, 1319 (1978).
[12] T. Markvart, J. Phys. C: Solid State Phys. **14**, L895 (1981).
[13] S. Nakamura, Science **281**, 956 (1998).
[14] A. G. Aberle, Prog. Photovoltaics Res. Appl. **8**, 473 (2000).
[15] L. Korte, E. Conrad, H. Angermann, R. Stangl, and M. Schmidt, Sol. Energy Mater. Sol. Cells **93**, 905 (2009).
[16] M. Schmidt, L. Korte, A. Laades, R. Stangl, C. Schubert, H. Angermann, E. Conrad, and K. v. Maydell, Thin Solid Films **515**, 7475 (2007).
[17] C. Ran, J. Xu, W. Gao, C. Huang, and S. Dou, Chem. Soc. Rev. **47**, 4581 (2018).
[18] D. W. deQuilettes, K. Frohna, D. Emin, T. Kirchartz, V. Bulovic, D. S. Ginger, and S. D. Stranks, Chem. Rev. **119**, 11007 (2019).
[19] Y. Rakita, I. Lubomirsky, and D. Cahen, Mater. Horizons **6**, 1297 (2019).
[20] H. Jin, E. Debroye, M. Keshavarz, I. G. Scheblykin, M. B. J. Roeffaers, J. Hofkens, and J. A. Steele, Mater. Horizons **7**, 397 (2020).
[21] A. Alkauskas, M. D. McCluskey, and C. G. Van De Walle, J. Appl. Phys. **119**, 181101 (2016).
[22] H. B. Bebb and R. A. Chapman, J. Phys. Chem. Solids **28**, 2087 (1967).
[23] H. B. Bebb, Phys. Rev. **185**, 1116 (1969).
[24] B. K. Ridley, J. Phys. C: Solid State Phys. **13**, 2015 (1980).
[25] T. Kirchartz and U. Rau, Adv. Energy Mater. **8**, 1703385 (2018).
[26] T. Kirchartz, L. Krückemeier, and E. L. Unger, APL Mater. **6**, 100702 (2018).
[27] T. Kirchartz, Philos. Trans. R. Soc., A **377**, 20180286 (2019).
[28] M. Yavari, F. Ebadi, S. Meloni, Z. S. Wang, T. C.-J. Yang, S. Sun, H. Schwartz, Z. Wang, B. Niesen, J. Durantini, P. Rieder,

K. Tvingstedt, T. Buonassisi, W. C. H. Choy, A. Filippetti, T. Dittrich, S. Olthof, J.-P. Correa-Baena, and W. Tress, J. Mater. Chem. A **7**, 23838 (2019).
[29] I. Levine, S. Gupta, A. Bera, D. Ceratti, G. Hodes, D. Cahen, D. Guo, T. J. Savenije, J. Ávila, H. J. Bolink, O. Millo, D. Azulay, and I. Balberg, J. Appl. Phys. **124**, 103103 (2018).
[30] D. Guo, V. M. Caselli, E. M. Hutter, and T. J. Savenije, ACS Energy Lett. **4**, 855 (2019).
[31] T. Walter, R. Herberholz, C. Müller, and H. W. Schock, J. Appl. Phys. **80**, 4411 (1996).
[32] T. S. Sherkar, C. Momblona, L. Gil-Escrig, J. Ávila, M. Sessolo, H. J. Bolink, and L. J. A. Koster, ACS Energy Lett. **2**, 1214 (2017).
[33] T. S. Sherkar, C. Momblona, L. Gil-Escrig, H. J. Bolink, and L. J. A. Koster, Adv. Energy Mater. **7**, 1602432 (2017).
[34] A. Alkauskas, C. E. Dreyer, J. L. Lyons, and C. G. Van De Walle, Phys. Rev. B **93**, 201304(R) (2016).
[35] S. Kim, S. N. Hood, and A. Walsh, Phys. Rev. B **100**, 041202 (2019).
[36] S. Kim, J. S. Park, and A. Walsh, ACS Energy Lett. **3**, 496 (2018).
[37] J. Li, Z. K. Yuan, S. Chen, X. G. Gong, and S. H. Wei, Chem. Mater. **31**, 826 (2019).
[38] S. G. Motti, D. Meggiolaro, S. Martani, R. Sorrentino, A. J. Barker, F. De Angelis, and A. Petrozza, Adv. Mater. **31**, 1901183 (2019).
[39] S. Kim, J. A. Márquez, T. Unold, and A. Walsh, arXiv:1912.07889.
[40] D. H. Fabini, M. Koerner, and R. Seshadri, Chem. Mater. **31**, 1561 (2019).
[41] R. E. Brandt, J. R. Poindexter, P. Gorai, R. C. Kurchin, R. L. Z. Hoye, L. Nienhaus, M. W. B. Wilson, J. A. Polizzotti, R. Sereika, R. Žaltauskas, L. C. Lee, J. L. Macmanus-Driscoll, M. Bawendi, V. Stevanović, and T. Buonassisi, Chem. Mater. **29**, 4667 (2017).
[42] R. E. Brandt, V. Stevanović, D. S. Ginley, and T. Buonassisi, MRS Commun. **5**, 265 (2015).
[43] B. Blank, T. Kirchartz, S. Lany, and U. Rau, Phys. Rev. Appl. **8**, 024032 (2017).
[44] P. W. Bridgman, Phys. Rev. **31**, 101 (1928).
[45] B. E. Pieters, Ph.D. thesis, The Technical University of Delft, 2008.
[46] B. E. Pieters, H. Stiebig, M. Zeman, and R. A. C. M. M. van Swaaij, J. Appl. Phys. **105**, 044502 (2009).
[47] M. G. De Greef, F. A. Rubinelli, and R. van Swaaij, Thin Solid Films **540**, 227 (2013).
[48] M. G. De Greef and F. A. Rubinelli, Phys. Status Solidi **252**, 170 (2015).
[49] B. K. Ridley, *Quantum Processes in Semiconductors*, 5th ed. (Oxford Science Publications, New York, 2013).
[50] N. J. Turro, V. Ramamurthy, and J. C. Scaiano, *Principles of Molecular Photochemistry: An Introduction* (University Science Books, Mill Valley, 2008).
[51] K. Peuker, R. Enderlein, A. Schenk, and E. Gutsche, Phys. Status Solidi B **109**, 599 (1982).
[52] M. G. Burt, J. Phys. C: Solid State Phys. **16**, 4137 (1983).
[53] M. G. Burt, J. Phys. C: Solid State Phys. **15**, L381 (1982).
[54] R. Pässler, Czechoslov. J. Phys. B **25**, 219 (1975).
[55] R. Pässler, Czechoslov. J. Phys. B **24**, 322 (1974).
[56] E. Gutsche, J. Lumin **24-25**, 689 (1981).
[57] A. Alkauskas, Q. Yan, and C. G. de Walle, Phys. Rev. B **90**, 075202 (2014).
[58] See Supplemental Material at http://link.aps.org/supplemental/10.1103/PhysRevMaterials.4.024602 for the different approaches available for calculation of capture coefficients, the overlap factor occurring in radiative transitions, validity of the model, capture coefficients, and the effect of the charge state.
[59] P. T. Landsberg, *Recombination in Semiconductors*, 1st ed. (Cambridge University Press, Cambridge, UK, 1991).
[60] T. Kirchartz, T. Markvart, U. Rau, and D. A. Egger, J. Phys. Chem. Lett. **9**, 939 (2018).
[61] D. W. Lozier, Ann. Math. Artif. Intell. **38**, 105 (2003).
[62] P. Virtanen, R. Gommers, T. E. Oliphant, M. Haberland, T. Reddy, D. Cournapeau, E. Burovski, P. Peterson, W. Weckesser, J. Bright, S. J. van der Walt, M. Brett, J. Wilson, K. J. Millman, N. Mayorov, A. R. J. Nelson, E. Jones, R. Kern, E. Larson, C. Carey, İ. Polat, Y. Feng, E. W. Moore, J. VanderPlas, D. Laxalde, J. Perktold, R. Cimrman, I. Henriksen, E. A. Quintero, C. R. Harris, A. M. Archibald, A. H. Ribeiro, F. Pedregosa, P. van Mulbregt, and SciPy 1. 0 Contributors, arXiv:1907.10121.
[63] M. Sendner, P. K. Nayak, D. A. Egger, S. Beck, C. Müller, B. Epding, W. Kowalsky, L. Kronik, H. J. Snaith, A. Pucci, and R. Lovrinčić, Mater. Horizons **3**, 613 (2016).
[64] L. D. Whalley, J. M. Frost, B. J. Morgan, and A. Walsh, Phys. Rev. B **99**, 085207 (2019).
[65] L. Wang, J. Semicond. **40**, 091101 (2019).
[66] J. S. Park, S. Kim, Z. Xie, and A. Walsh, Nat. Rev. Mater. **3**, 194 (2018).
[67] W. Li, A. S. Vasenko, J. Tang, and O. V. Prezhdo, J. Phys. Chem. Lett. **10**, 6219 (2019).